Photocatalytic O$_2$ activation and reactive oxygen species evolution by surface B-N bond for organic pollutants degradation

Haiyin Zhan [a], Qixing Zhou [a,*], Mingmei Li [a], Ruiren Zhou [b], Yueshuang Mao [a], Pengfei Wang [a,c,**]

[a] *Ministry of Education Key Laboratory of Pollution Processes and Environmental Criteria, College of Environmental Science and Engineering, Nankai University, Tianjin 300350, China*
[b] *Department of Biological and Agricultural Engineering, Texas A&M University,126 Hobgood, 2117 TAMU, College Station, TX 77843-2117, USA*
[c] *School of Energy and Environmental Engineering, Hebei University of Technology, Tianjin 300401, China*

ARTICLE INFO

ABSTRACT

The efficiency of photocatalytic molecular oxygen (O$_2$) activation is limited by the poor O$_2$ adsorption and the obstruction of electron transfer. Herein, we designed a graphite carbon nitride with surface B-N bond (B$_x$-C$_3$N$_4$) to improve its efficiency. A series of characterizations and DFT calculations show that boron atom replaces carbon atom to form B-N bond, which increase the O$_2$ adsorption energy from − 0.47 eV to − 1.17 eV. Moreover, the doped boron atom can be used as the electron capture center to transfer electrons to the N atom, then to the surface adsorbed O$_2$ through the N-O bond, thus improving the photocatalytic generation of·O$_2^-$ and ^{1}O$_2$. Finally, the photocatalytic degradation rates of RhB, tetracycline and o-nitrophenol by B$_{0.05}$-C$_3$N$_4$ are 12.3, 4.8 and 18.5 times that of pure g-C$_3$N$_4$, respectively. Moreover, the degradation pathway and toxicity prediction of intermediates of RhB are proposed based on the results of HPLC-MS and DFT calculations.

1. Introduction

The control and treatment of water pollution has become an urgent and important task in the process of social development [1,2]. Therefore, it is urgent to find a new efficient sewage treatment technology in the face of more complex water pollution conditions [3]. As we all know, molecular oxygen (O$_2$) as the greenest and cheapest oxidant widely exists in various environmental media including water. Unfortunately, due to the limitation of the spin-forbidden reaction, most organic pollutants cannot be directly oxidized [4]. Hence, how to transform the O$_2$ into reactive oxygen species (ROS) with stronger oxidizing ability has become the focus of our attention. Photocatalytic O$_2$ activation technology has attracted extensive attention because of its green and high efficiency [5]. Photocatalysts are excited by light to generate photogenerated electrons, which convert O$_2$ to ROS by transferring electrons or energy to O$_2$ [6], including superoxide anion radical (·O$_2^-$) [7], singlet oxygen (^{1}O$_2$) [8], hydroxyl radicals (·OH) and hydrogen peroxide (H$_2$O$_2$) [9], etc. These highly oxidizing ROS can attack and degrade pollutants to achieve sewage purification effect.

Graphitic carbon nitride (g-C$_3$N$_4$) has attracted extensive research in the field of photocatalysis due to its safety, cheapness, and high visible light response, making it a promising candidate for photocatalytic water purification [10]. Nevertheless, the photocatalytic efficiency of pure g-C$_3$N$_4$ is not satisfactory due to its fast photogenerated electron-hole recombination rate, low utilization of visible light, and small specific surface area [11]. In order to overcome the above shortcomings, there have been a lot of researches to improve the photocatalytic efficiency of g-C$_3$N$_4$ based catalysts through the construction of heterostructures [12, 13], element doping [14,15], surface modification [16,17] and other methods. However, there are few studies on surface bonding to enhance photocatalytic O$_2$ activation. Zhou et al. constructed Ag-N bond as electron transfer channel in g-C$_3$N$_4$, which promoted electron transfer and improved the ability of photocatalytic activation of O$_2$ [18]. Similarly, Xiao et al. introduced the Cu-N bond into the in-plane and interlayer of g-C$_3$N$_4$ to generate a new charge transfer channel. The results show that Cu-N can greatly improve the in-plane and interlayer

separation/transfer of charge carriers, thus improving the photocatalytic efficiency [19]. It can be seen that the formation of surface chemical bonds by metal doping can significantly improve the photocatalytic performance of g-C$_3$N$_4$, but metal doping always has the risk of metal leakage [20]. Although the doping ratio is low, its ecological impact in the actual water treatment process is worthwhile considerate.

The introduction of surface chemical bonds formed by doping of non-metallic elements can avoid the ecological impact of metal leakage. As the basic element of the origin of life, boron has the advantages of green, safety and low price [21]. More importantly, boron dopants can introduce B-N bonds into g-C$_3$N$_4$, which have the characteristics of hexagonal boron nitride (h-BN) such as sp^2 hybridization and ionic characteristics, which can effectively change the electronic structure and photoelectrical properties of g-C$_3$N$_4$ [22]. The introduction of B-N bond can effectively reduce the lowest unoccupied molecular orbital (LUMO)/the highest occupied molecular orbital (HOMO) energy levels of the semiconductor, making electron transition easier and more favorable for photocatalytic reaction [23,24]. The bond can effectively promote charge separation and electron transfer, and more electrons and energy are transferred to the surface adsorbed oxygen through the B-N bond, which can improve the ability of photocatalytic O$_2$ activation. Currently, the mechanism of the introduction of surface B-N bond to enhance photocatalytic O$_2$ activation is rarely researched.

Herein, we designed and synthesized g-C$_3$N$_4$ photocatalyst with surface B-N bond to promote its ability of photocatalytic O$_2$ activation to produce ROS, and applied it to photocatalytic degradation of organic pollutants (Rhodamine B (RhB), tetracycline and o-nitrophenol). The introduction of B-N bond not only improves the light absorption capacity and charge separation efficiency of g-C$_3$N$_4$, but also acts as the adsorption site of O$_2$ and electron transfer channel to accelerate electron transfer, thus improving the ROS generation efficiency of the catalyst. Based on the efficient production of ROS, the degradation efficiency of RhB, tetracycline and o-nitrophenol is 12.3, 4.8 and 18.5 times of pure g-C$_3$N$_4$, respectively. Simultaneously, the rational charge transfer mechanism in photocatalytic O$_2$ activation and the degradation mechanism and degradation path of pollutants were investigated in detail. In addition, we simulated the actual wastewater by setting different water environmental parameters (solution pH, organic matter and inorganic anion), which further verified the application prospect of B$_x$-C$_3$N$_4$ in the actual water treatment process.

2. Experimental section

All chemicals were used directly without further purification and were all analytic reagents. Deionized water was used in all experiments.

2.1. Synthesis of pure g-C$_3$N$_4$

Pure g-C$_3$N$_4$ was synthesized in one step by thermal polymerization using melamine as the precursor. In detail, 5 g of melamine powder was put into a crucible with a lid, and heated to 520 ℃ in a muffle furnace at a heating rate of 5 ℃/min for 4 h. After the crucible was cooled, the yellow pure g-C$_3$N$_4$ was gathered and attrite for further use.

2.2. Synthesis of g-C$_3$N$_4$ with surface B-N bond

NaBH$_4$ was physically mixed with pure g-C$_3$N$_4$ and then calcined under an inert gas to obtain g-C$_3$N$_4$ with surface B-N bond. Specifically, put 1 g of pure g-C$_3$N$_4$ and a certain ratio (mass ratio) of NaBH$_4$ into a mortar, and ground thoroughly for a few minutes until they were evenly mixed. The mixture was placed in a nitrogen-protected tube furnace, heated to 400 °C at a temperature increase rate of 10 °C per minute, and calcined for 4 h. After the tube furnace was naturally cooled, the sample was taken out and rinsed several times with deionized water and ethanol to remove unreacted NaBH$_4$ and other impurities. Then the cleaned sample was dried overnight in a vacuum drying oven at 80 ℃ to obtain

g-C$_3$N$_4$ with surface B-N bond. The obtained sample were denoted as B$_x$-C$_3$N$_4$ (x is the mass ratio of boron atom in NaBH$_4$ to pure g-C$_3$N$_4$, x = 0.01, 0.03, 0.05, 0.07, 0.1).

2.3. Photocatalytic degradation experiments

Using RhB as the probe pollutant, the photocatalytic degradation performance of the sample was estimated by degrading RhB (20 mg/L) simulated wastewater under visible light. The light source is 300 W Xenon lamp (CEL-HXF300) with a ultraviolet (UV) cut-off filter (λ < 420 nm). In a representative photocatalysis experiment, 40 mg of photocatalyst was dispersed in 100 mL of RhB solution and stirred in darkness for 30 min to attain the adsorption and desorption equilibrium. Irradiated at the same time interval, 3 mL suspension was taken and filtered, and its absorbance was measured by UV–visible (vis) spectrophotometer (the maximum absorption wavelength of RhB is 554 nm) to determine the remaining concentration of pollutants. RhB residues and degraded intermediates were determined by high performance liquid chromatography-mass spectrometry (HPLC-MS, Orbitrap Fusion, Thermo, USA), the eluent consisted of 0.1% formic acid and acetonitrile at a flow rate of 0.2 mL/min. The degradation process of tetracycline and o-nitrophenol was evaluated by HPLC.

2.4. O$_2$ activation measurements

20 mg of the prepared material was mixed with 0.4 mL of 3,3′,5,5′-tetramethylbenzidine (TMB, 50 mM) and 40 mL of HAc/NaAc buffer solution. The light source and experimental procedure are consistent with photocatalytic degradation experiments. TMB oxidation were estimated by UV–vis spectrophotometer (the maximum absorption wavelength is around 370 nm) at different time intervals.

Details of material characterization, calculation methods, and photoelectric chemical measurement methods were given in supporting information Text S1.

3. Results and discussion

3.1. Morphology and structure of the photocatalysts

In this work, pure g-C$_3$N$_4$ was synthesized in one step by thermal polymerization with melamine as the precursor, and then g-C$_3$N$_4$ with B-N bond on the surface was obtained by physical mixing NaBH$_4$ and pure g-C$_3$N$_4$ and calcination under nitrogen (Fig. 1a). The samples were denoted as B$_x$-C$_3$N$_4$, and B$_{0.05}$-C$_3$N$_4$ was picked as the typical sample because of the best performance. The morphology and microstructure of the synthetic samples were observed by transmission electron microscopy (TEM) and energy-dispersive X-ray spectroscopy (EDS) mapping profiles (Fig. 1b and Fig. S1). For pure g-C$_3$N$_4$, the sample has a sheet structure and uniform element distribution. After the introduction of boron atoms, the sample maintains the sheet structure and the surface becomes more rough and wrinkled, which provides more adsorption and reaction sites for photocatalytic degradation of pollutants. The boron atoms are evenly distributed in the EDS mapping profiles, indicating that the B atoms are successfully introduced.

The chemical structures and surface groups of pure g-C$_3$N$_4$ and B$_{0.05}$-C$_3$N$_4$ were characterized by X-ray diffraction (XRD) patterns and fourier transform infrared (FT-IR) spectra. As shown in Fig. 1c, the pure g-C$_3$N$_4$ exhibits two XRD diffraction peaks at 2θ= 13.1° and 27.3°, corresponding to (100) planar repeated tri-s-trizine (heptazine) units and (002) interlayer superimposed motifs respectively (as shown in the illustration) [25]. The intensity of the XRD diffraction peaks of B$_{0.05}$-C$_3$N$_4$ is weaker than pure g-C$_3$N$_4$, indicating that the introduction of B atoms influences the growth of g-C$_3$N$_4$ crystal plane and the ordered structure in the frame [26]. The FT-IR spectra (Fig. 1d) display that pure g-C$_3$N$_4$ and B$_{0.05}$-C$_3$N$_4$ have similar absorption peaks at 810 cm^{-1}, 1100–1700 cm^{-1} and 3200 cm^{-1}, which are attributed to bending
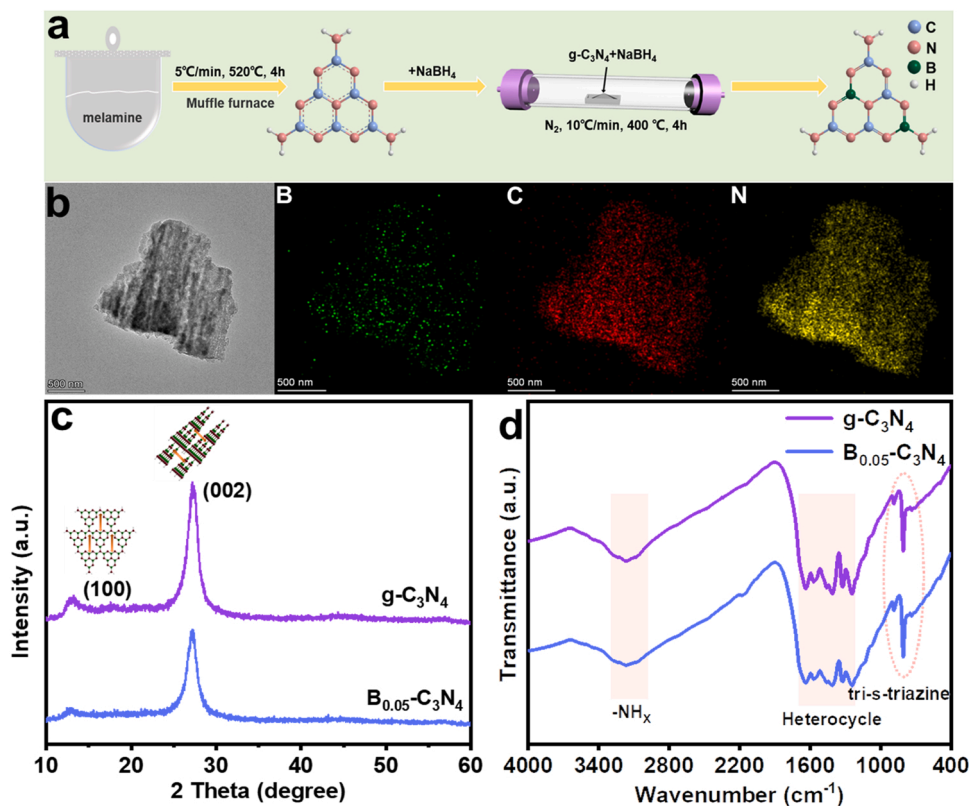
Fig. 1. (a) Schematic illustration for the synthesis of B_x-C_3N_4 composite photocatalysts. (b) TEM images of $B_{0.05}$-C_3N_4 and corresponding element mapping for B, C, N. (c) XRD patterns and (d) FT-IR spectra of the prepared samples.

vibration of triazine ring, stretching vibration of C-N heterocyclic ring and -NH$_X$ group, respectively [18,27]. It is worth noting that the C-N heterocyclic vibration peak of $B_{0.05}$-C_3N_4 is significantly weaker than that of pure g-C_3N_4, which may be caused by the change of C-N lattice structure caused by B atoms doping [28]. To sum up, the introduction of B atoms did not cause serious damage to the original structure of g-C_3N_4, as can be seen from XRD and FT-IR spectra. In addition, similar raman

spectra (Fig. S2) can also illustrate this point.

To confirm the presence of B-N bond and further determine the local structure of the synthesized materials, the chemical states of B, C, N and O elements were studied by X-ray photoelectron spectroscopy (XPS) spectra. In the C 1 s high-resolution spectrum of pure g-C_3N_4 and B_x-C_3N_4 (Fig. 2a), the binding energy peaks of 284.8 eV and 288.2 eV are attributed to the standard reference carbon and N-C≡N in the typical
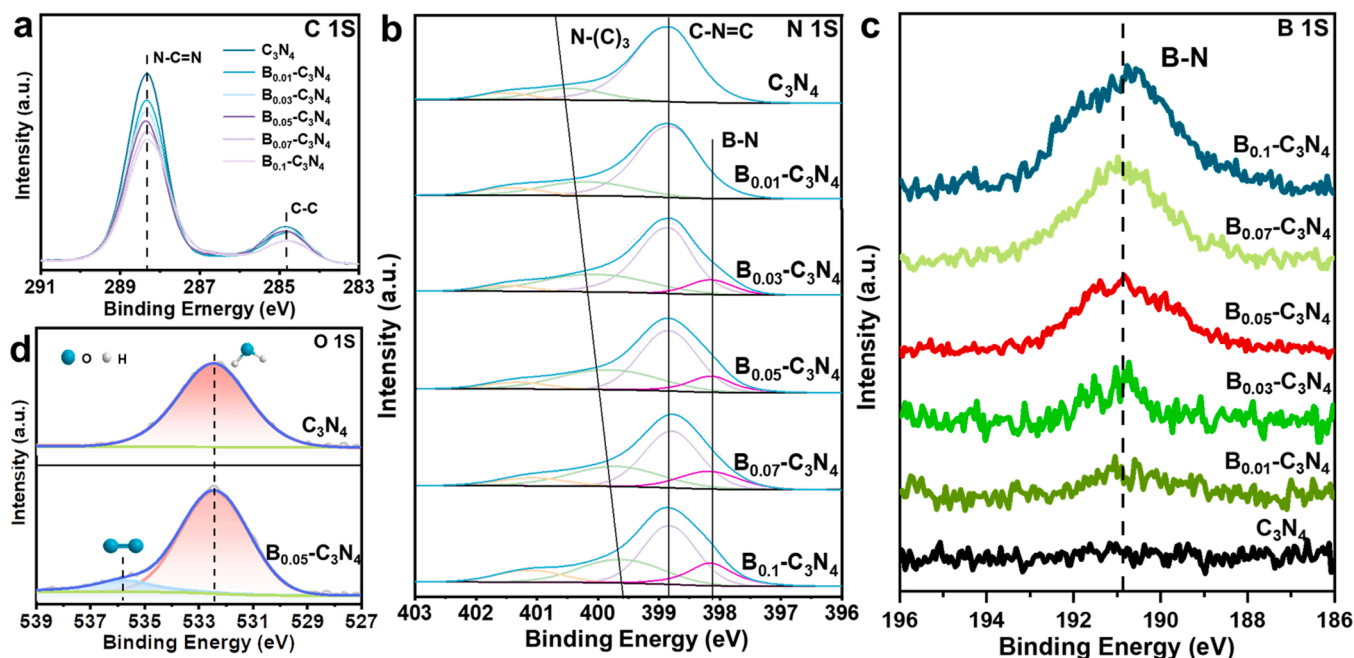

Fig. 2. The high-resolution XPS spectra of pure g-C_3N_4 and B_x-C_3N_4: (a) C 1 s, (b) N 1 s, (c) B 1 s, (d) O 1 s.

heterocyclic ring, respectively [29]. It is worth noting that the peak intensity of N-C≡N decreases gradually with the increasing doping amount of B atoms, indicating that a certain amount of N-C≡N is replaced by the bonding of B atoms introduced [30]. In addition, no peak was found at binding energy of 283.5 eV, which ruled out the possibility of B-C bond formation, indicating that B atoms doping may replace C atoms in g-C_3N_4 structure [31]. As shown in the N 1 s high-resolution spectra of pure g-C_3N_4 and B_x-C_3N_4 (Fig. 2b), three well-resolved peaks appear near the binding energies of 398.8 eV, 399.9 eV and 401.2 eV, which are due to the binding energy peaks generated by C-N≡C, N-(C)$_3$ and -NH$_X$ structure [32–34]. Interestingly, the N-(C)$_3$ structure characteristic peak gradually moves to the direction of low binding energy with the increase of B atoms doping, which is mainly due to the fact that N-(C)$_3$ captures more electrons when boron atoms are doped in the bay site [30]. It is worth noting that in all the N 1 s high-resolution spectrum of B_x-C_3N_4, the characteristic peak of the B-N bond is found at a binding energy of about 398.0 eV, indicating the B-N bond was formed (except for $B_{0.01}$-C_3N_4, it may be due to low doping). In the B 1 s high resolution spectrum of pure C_3N_4 and B_x-C_3N_4 (Fig. 2c), the intensity of the characteristic peak of B-N bond around 190.8 eV increases with the doping amount of B atoms, further proving B-N bond was introduced into the catalyst [35]. To explore the effect of B-N bond on the oxygen adsorption capacity of g-C_3N_4, we tested the high resolution spectra of O 1 s of pure g-C_3N_4 and $B_{0.05}$-C_3N_4 (Fig. 2d). As expected, no characteristic peak of lattice oxygen is found near 529.0 eV in the O 1 s spectrum of pure g-C_3N_4 and $B_{0.05}$-C_3N_4, and the characteristic peak of adsorbed water molecule appeares near 532.2 eV. Interestingly, a new peak of binding energy appears at about 535.6 eV for $B_{0.05}$-C_3N_4, which could be attributed to the peak of O_2 adsorbed on the surface, indicating that the introduction of the B-N bond promotes the O_2 adsorption capacity of g-C_3N_4 [36].

To further determine the molecular structure of the sample and the boron doping site, we performed [11]B and ^{13}C cross-polarization magic angle spinning nuclear magnetic resonance (CP-MAS NMR) tests on the sample. As shown in the ^{11}B NMR spectrum of $B_{0.05}$-C_3N_4 (Fig. 3a), two boron signals representing different doping sites can be seen, namely corner boron (B_1) and bay boron (B_2) (as illustrated in Fig. 3a) [37]. In Fig. 3b, the ^{13}C NMR spectra of pure g-C_3N_4 and $B_{0.05}$-C_3N_4 showe two strong peaks near 158.8 ppm and 164.9 ppm. The peak at δ ≈ 158.8 ppm is mainly related to the C at position 1 in the illustration, that is, the carbon atom in C-(N)$_3$. The peak at δ ≈ 164.9 ppm corresponds to the carbon at position 2 in the illustration, which is the C in the carbon atom of $CN_2(NH_x)$ [38]. According to CP-MAS NMR, the formation process of B-N bond seems to be mainly due to the heat treatment of $NaBH_4$, which causes boron atoms to replace carbon atoms in the triazine ring and form B-N bonds with adjacent nitrogen atoms. Electron

paramagnetic resonance (EPR) can assess direct information on various behaviors of natural defects such as nitrogen vacancies [39]. As shown in Fig. 3c, both of pure g-C_3N_4 and $B_{0.05}$-C_3N_4 reveal one single Lorentzian line with a g value of 2.004, which can be attributed to the electrons trapped in N vacancies. The stronger Lorentzian signal of $B_{0.05}$-C_3N_4 indicates that the introduction of B-N bond increases the concentration of N vacancies in the catalyst, which is beneficial for light absorption and space charge separation [40]. The Brunner-Emmet-Teller (BET) measurement results of pure g-C_3N_4 and $B_{0.05}$-C_3N_4 are shown in Fig. S3, table S1 and S2. The BET specific surface areas of $B_{0.05}$-C_3N_4 and pure g-C_3N_4 are 10.3591 $m^2 \cdot g^{-1}$ and 5.7880 $m^2 \cdot g^{-1}$, respectively. There is little difference between the specific surface area of $B_{0.05}$-C_3N_4 and pure g-C_3N_4, so the surface B-N bond instead of the specific surface area is the main reason for enhancing the O_2 adsorption capacity of $B_{0.05}$-C_3N_4.

3.2. Degradation of organic pollutants

We used RhB as a probe pollutant to estimate the ability of pure g-C_3N_4 and $B_{0.05}$-C_3N_4 to degrade organic pollutants in wastewater. The photocatalytic degradation curves of RhB by synthetic photocatalysts are shown in Fig. 4a, the adsorption of RhB on pure g-C_3N_4 and $B_{0.05}$-C_3N_4 is small in dark condition. In the process of one hour of light exposure, the degradation efficiency of RhB by $B_{0.05}$-C_3N_4 significantly improved. To be specific, the degradation rate of RhB by pure g-C_3N_4 is about 27.4% in 60 min, and the degradation rate of $B_{0.05}$-C_3N_4 is the highest in the same time, reaching 100%. As shown in Fig. S4, all the curves fit well with the pseudo-first-order kinetic equation (-ln (C/ C_0)= κt), indicating that the degradation process conforms to the pseudo-first-order reaction kinetics. The correlation coefficient (R^2) and pseudo first-order rate constant (κ) were calculated as shown in Table S3. It is not difficult to see that in all the prepared samples, $B_{0.05}$-C_3N_4 has the highest value of κ (0.0627 min^{-1}), which is about 12.3 times of pure g-C_3N_4. In order to demonstrate the good degradation effect of g-C_3N_4 with surface B-N bond, we compared the photocatalytic degradation efficiency of TiO_2 (P25) reference photocatalyst (Fig. S5) and other similar studies (Table S4), and the results showed that our photocatalyst has excellent degradation effect.

In order to explore the reasons for the degradation of pollutants, we introduce a series of sacrificial agents into the reaction system to determine the active species. A certain concentration of superoxide dismutase (SOD) (200 units/mL), isopropanol (2 mmol/L), β-carotene (0.2 mmol/L), catalase (200 units/mL), $AgNO_3$ (0.5 mmol/L), EDTA-2Na (1 mmol/L) was added to the photocatalytic reaction system to capture·O_2^-,·OH, $^1O_2$, H_2O_2, e^-, h^+, respectively. As shown in Fig. 4b, the photodegradation efficiency of RhB was significantly inhibited after the
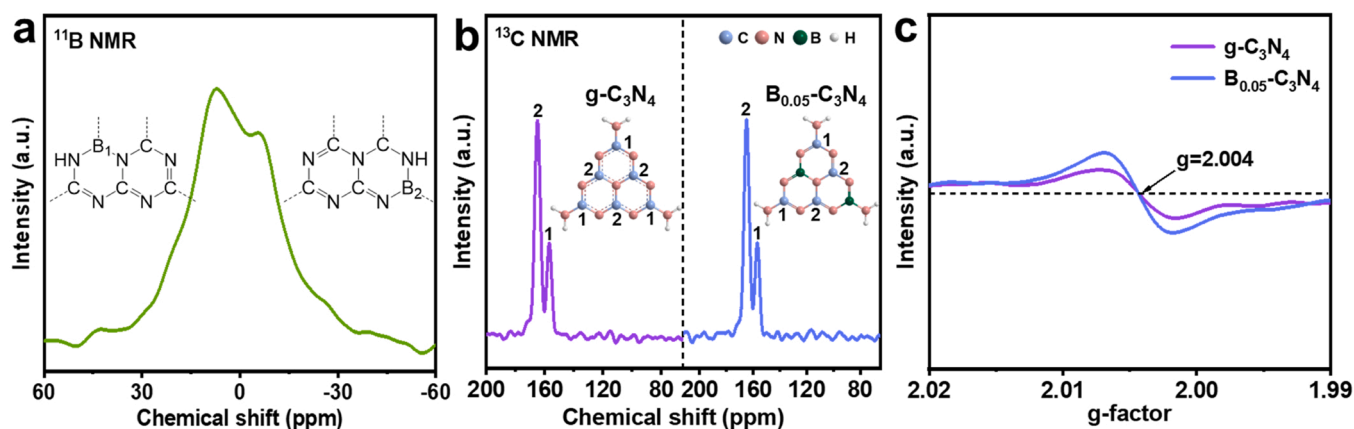

Fig. 3. (a) Solid-state ^{11}B CP-MAS NMR spectrum of $B_{0.05}$-C_3N_4. (b) Solid-state ^{13}C CP-MAS NMR spectra of pure g-C_3N_4 and $B_{0.05}$-C_3N_4. (c) EPR spectra of pure g-C_3N_4 and $B_{0.05}$-C_3N_4.
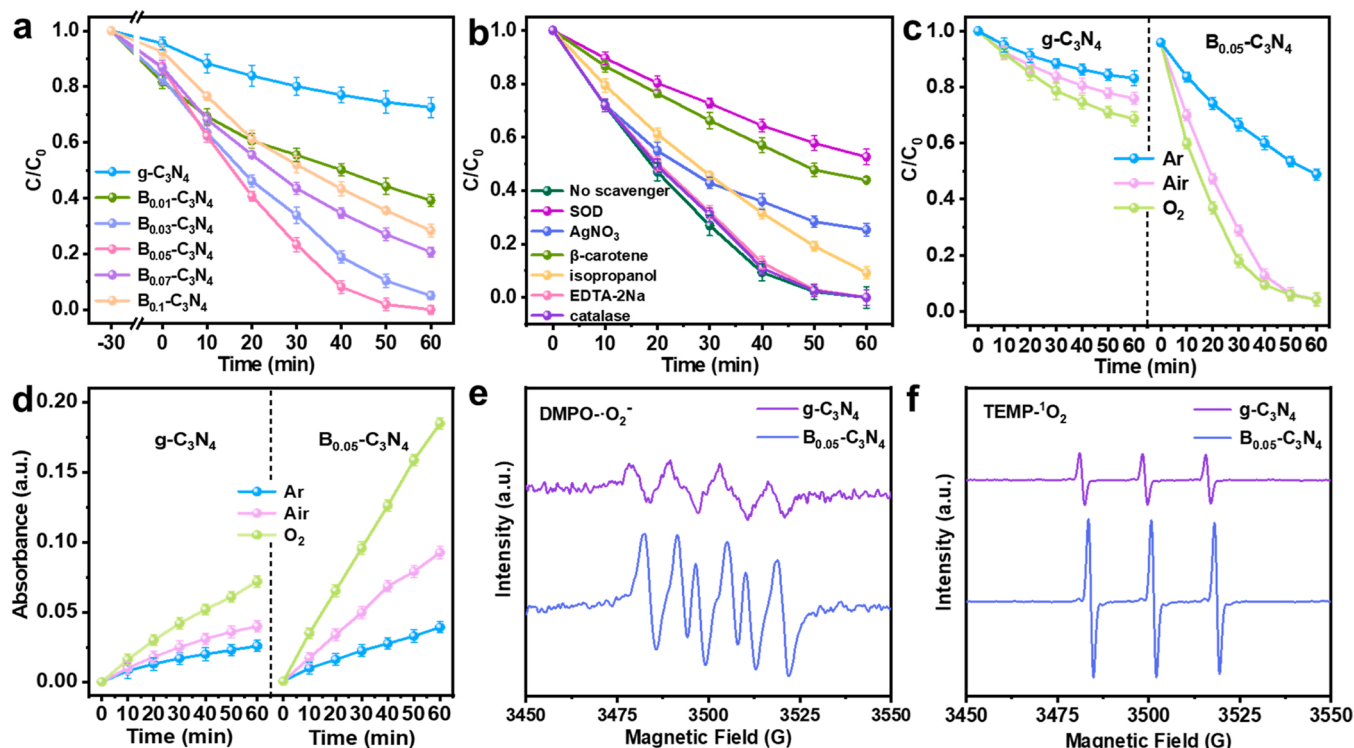
Fig. 4. (a) The degradation efficiency of the prepared sample (400 mg/L) on RhB (20 mg/L) under visible light irradiation was investigated. (b) The photocatalytic degradation efficiencies of RhB (20 mg/L) by $B_{0.05}$-C_3N_4 (400 mg/L) with different scavengers. (c) Photocatalytic degradation of RhB (20 mg/L) by pure g-C_3N_4 and $B_{0.05}$-C_3N_4 in different gas conditions. (d) The product absorbance peak monitored at 370 nm versus reaction time under different gas conditions for pure g-C_3N_4 and $B_{0.05}$-C_3N_4. The ESR spectra of·O_2^- and $^1O_2$ of pure g-C_3N_4 and $B_{0.05}$-C_3N_4 were studied by using DMPO and TEMP as free radical collectors respectively in (e) and (f). Error bars represent standard deviations from triplicate experiments (n = 3).

addition of SOD, β-carotene, and AgNO₃, but no conspicuous inhibition was discovered after the addition of isopropanol, catalase and EDTA-2Na. The above results indicate that·O_2^-, $^1O_2$, and e⁻ play a major role in the RhB degradation. To verify the importance of O_2 in the reaction system, we studied the effect on the catalytic reaction rate by controlling the concentration of dissolved oxygen in the reaction system. Specifically, O_2 is introduced into the reaction system to increase the concentration of dissolved O_2 in the reaction system, and inert gas (Ar) is introduced to exhaust the dissolved O_2 in the system to reduce the concentration of dissolved O_2. Firstly, the influence of oxygen concentration on the photocatalytic degradation of RhB was explored. As shown in Fig. 4c, when inert gas was introduced to reduce the dissolved oxygen concentration, the degradation of RhB by $B_{0.05}$-C_3N_4 is significantly inhibited. The degradation rate was improved to a certain extent when the concentration of dissolved oxygen was increased by the introduction of oxygen, which fully demonstrated the importance of oxygen molecules in the photocatalytic degradation of pollutants. On this basis, we used TMB as a probe molecule to detect the O_2 activation characteristics of $B_{0.05}$-C_3N_4 (Fig. 4d). The oxidation capacity of $B_{0.05}$-C_3N_4 to TMB was significantly increased than pure g-C_3N_4 and showed a high degree of O_2 dependent oxidation characteristics, indicating that the active substances of TMB oxidation were mainly related to the O_2 activation. To provide direct evidence of the ROS generated by the photocatalytic activation of O_2, we performed an electron spin resonance (ESR) test. 5,5-dimethyl-1-pyrroline N-oxide (DMPO) and 2,2,6,6-Tetramethylpiperidine (TEMP) were used as capture agents to detect the production of·O_2^- and $^1O_2$ respectively. As shown in Fig. 4e and f, the sextet peaks and triplet peaks (the ESR characteristic signals of·O_2^- and $^1O_2$) of $B_{0.05}$-C_3N_4 are significantly stronger than those of pure g-C_3N_4. These results not only provide conclusive evidence for the generation of·O_2^- and $^1O_2$, but also confirm that the introduction of B-N bond enhances the ability of photocatalytic activation of O_2 to generate·O_2^- and

$^1O_2$. In addition, ESR was used to detect the generation of·OH as shown in Fig. S6, the characteristic quadruple peak with the 1:2:2:1 intensity ratio of·OH is not found under visible light irradiation. The ESR test results were consistent with quenching test. Therefore, we can speculate on the process of ROS generation. First, the catalyst generates photo-generated electrons through light excitation, and the O_2 adsorbed on the catalyst surface captures the photo-generated electrons to generate·O_2^-. There are two main ways to produce $^1O_2$, one is the energy transfer from the excited photocatalyst to the triplet ground state of oxygen, and the other is generated from the oxidation of·O_2^- by hole [41]. The quenching experiment results show that h⁺ has no obvious effect on the reaction system, so the production of $^1O_2$ tends to be the first way of production.

In the actual process of organic pollution wastewater treatment, the pH value of sewage, dissolved natural organic matter, anions and other factors will affect the photocatalytic effect. The pH value of the solution may inhibit or enhance the photocatalytic degradation by influencing the surface electrons of the catalyst and ROS generation. In addition, the deliquescent organics or anions in the actual polluted wastewater may influence the photodegradation efficiency by competing with the pollutants for adsorption sites or expending ROS [42]. Therefore, to test the universal applicability of $B_{0.05}$-C_3N_4 in practical applications, we investigated the influence of factors such as pH, humic acid (HA), and HCO_3^- in the actual water environment on the degradation of RhB by $B_{0.05}$-C_3N_4. Firstly, 0.1 M HCl or NaOH was used to adjust the initial pH of the reaction system to investigate the influence of pH on the degradation of RhB by $B_{0.05}$-C_3N_4. As shown in Fig. S7a, the degradation of RhB was promoted by acidic environment and inhibited by alkaline environment. This may be attributable to the fact that when the pH of the reaction system is less than 4.8, the oxidation-reduction potential of O_2/•O_2^- becomes more positive, making O_2 easier to be reduced to •O_2^-, which promotes the degradation of pollutants. Under alkaline

conditions, more OH⁻ due to the charge repulsion effect may affect the transfer of photo-generated electrons on the catalyst surface, thereby affecting the generation of ROS and inhibiting the degradation rate. All in all, $B_{0.05}$-C_3N_4 showed a high degree of adaptability at different pH values. Secondly, humic acid (HA) was used to investigate the influence of dissolved natural organic matter in water. Different concentrations of HA produced a slight inhibitory effect on the degradation of RhB in Fig. S7b. As the concentration increased, the degree of inhibition increased correspondingly, which was caused by the competition between HA and RhB for ROS during the degradation process. Finally, HCO_3^- as a representative of inorganic anion was used to study its effect on the photocatalytic degradation of RhB. The effect of HCO_3^- on RhB degradation was negligible, as can be seen from Fig. S7c. In general, $B_{0.05}$-C_3N_4 is less affected by environmental factors in actual water, and it is promising to be used in actual wastewater treatment. Considering the cost of catalyst, we explored the effect of catalyst dosage on RhB photocatalytic degradation. As shown in Fig. S7d, when the dosage of the catalyst was less than 400 mg/L, the photocatalytic efficiency was significantly improved with the increase of the dosage. When the dosage of the catalyst exceeded 400 mg/L, the photocatalytic degradation efficiency did not improve obviously with the increase of the amount of catalyst. Therefore, we recommend the best dosage of catalyst is 400 mg/L to consider the economics of water treatment. In addition, considering the photosensitivity of dyes, the photocatalytic capacity of pure g-C_3N_4 and $B_{0.05}$-C_3N_4 to other non-dye-based organic pollutants (tetracycline and o-nitrophenol) was investigated (Fig. S8). It is not difficult to see that the photocatalytic degradation efficiency of g-C_3N_4 with sueface B-N bond is significantly improved, and the degradation rate is 4.8 times and 18.5 times of pure g-C_3N_4, respectively.

3.3. Mechanism of photocatalytic O_2 activation

To clarify the reasons for enhancing photocatalytic O_2 activation, the four basic processes of oxygen adsorption on the catalyst surface, light absorption, charge separation and transfer, and activation of interfacial adsorbed O_2 were considered [36].

We first considered the chemical adsorption of O_2 on the material surface, which is the premise in the catalytic reaction. The influence of B-N bond on the ability of pure g-C_3N_4 to adsorb O_2 was studied by Density functional theory (DFT) calculations. As shown in Fig. 5a, the interaction between pure g-C_3N_4 and O_2 is weak and no obvious chemical bond is formed. After the B-N bond was introduced, O_2 forms a strong covalent interaction with the N atom in the B-N bond (bay boron doping site rather than corner boron site) (Fig. 5b), and the adsorption energy is − 0.47 eV and − 1.19 eV (Table S5), respectively. The results show that the introduction of B-N bonds caused by the doping of boron atoms significantly promotes the adsorption ability of the catalyst for O_2. Secondly, the light absorption capacity and band gap of the sample obtained were analyzed by UV–vis diffuse reflectance spectroscopy. In Fig. 5c, the absorption edge of pure g-C_3N_4 is 451.4 nm. Nevertheless, when the B-N bond was introduced into the g-C_3N_4 framework, the absorption edge of $B_{0.05}$-C_3N_4 undergoes a slight red shift, reaching 476.8 nm. This phenomena can be reasonably attributed to the appearance of B-N bond and the increase of π electron delocalization in the conjugated system [43]. The optical band gap of the sample can be deduced from the Tauc diagram and Kubelka Monk theory. The band gap of $B_{0.05}$-C_3N_4 narrows from 2.54 eV of pure g-C_3N_4 to 2.43 eV (Fig. 5d), which may be attributed to the substitution of C atoms in the g-C_3N_4 framework by B atoms, thus affects the transitions between the weakly localized π–π * states that stem from the sp^2 hybridization of C and N in the g-C_3N_4 framework [44]. To determine the valence band positions of pure g-C_3N_4 and $B_{0.05}$-C_3N_4, we performed valence band (VB) XPS characterization. As shown in Fig. 5e, the maximum values of pure g-C_3N_4 and $B_{0.05}$-C_3N_4 valence bands are 1.88 eV and 1.66 eV, respectively. After the measurement error is eliminated by VB (vs NHE)$= \Phi + VB_{max}$-4.44 (the work function (Φ) of XPS analyzer and vacuum level to be 3.88 and 4.44 eV (vs NHE)) [26], the VB positions of pure g-C_3N_4 and $B_{0.05}$-C_3N_4 were 1.32 eV and 1.10 eV (vs NHE), respectively. Combining their band gaps, the conduction band (CB) positions of pure g-C_3N_4 and $B_{0.05}$-C_3N_4 can be determined to be
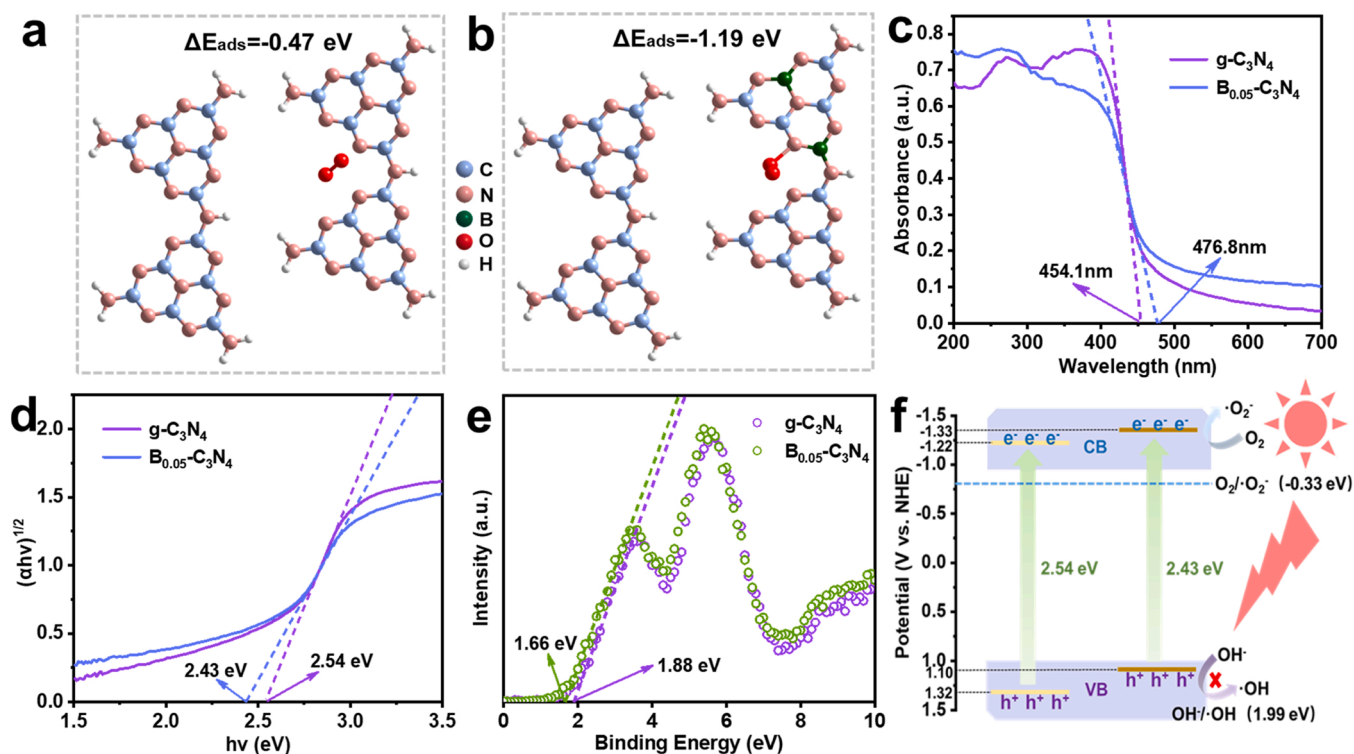
Fig. 5. Crystal structures of O_2 absorbed on pure g-C_3N_4 (a) and $B_{0.05}$-C_3N_4(b). (c) UV–vis diffuse reflectance spectra and (d) band-gap energy of pure g-C_3N_4 and $B_{0.05}$-C_3N_4. (e) VB XPS spectra and (f) schematic diagram of band structure of pure g-C_3N_4 and $B_{0.05}$-C_3N_4. 0.

− 1.22 eV and − 1.33 eV (vs NHE) (Fig. 5f). $B_{0.05}$-C_3N_4 has a more negative conduction band position than the oxidation-reduction potential of $O_2/\bullet O_2^-$ (−0.33 eV), providing the necessary conditions for the generation of·O_2^-, which is in keeping with the ESR test results.

The separation efficiency of the electron-hole pairs and the lifetime of the photo-generated charge of the catalyst were evaluated by steady-state photoluminescence (PL) and time-resolved PL experiments (Fig. 6a and Fig. 6b). As shown in Fig. 6a, for pure g-C_3N_4, the spectrum shows a strong emission peak at 472 nm, which originates from the inter-band recombination of electrons and holes. The PL intensity is significantly reduced after the B-N bond was introduced, meaning the recombination of electrons and holes is effectively suppressed. This is mainly due to the introduction of B-N bond to form an internal electric field, which is conducive to the effective separation of photogenerated electrons and holes [45,46]. The time-resolved PL spectra reveals the characteristics of the photo-induced charge carriers of the sample (Fig. 6b and Table S6). In Table S6, τ_1, τ_2, and τ_3 are caused by charge transfer, electron capture, and the slow recombination of electron-hole pairs, respectively. The PL average lifetime (τ) is derived from the following Eq. (1):

$$(\tau) = \frac{A_1\tau_{1+}^2 A_2\tau_{2+}^2 A_3\tau_{3...}^2}{A_1\tau_1 + A_2\tau_2 + A_3\tau_{3...}} \tag{1}$$

It is calculated that the PL average lifetime of the samples has dropped from 27.38 ns for pure g-C_3N_4 to 22.05 ns for $B_{0.05}$-C_3N_4. Generally, the shorter PL average lifetime signifies the more satisfying and efficacious separation of charge carrier. The shorter PL average lifetime of $B_{0.05}$-C_3N_4 indicates that the B-N bond as an electron transport channel brings more convenient charge separation and transfer [47, 48]. It is not difficult to see from Fig. 6 that the photocurrent intensity corresponding of $B_{0.05}$-C_3N_4 is significantly stronger than pure g-C_3N_4, manifesting that the introduction of B-N bond promotes the separation and migration efficiency of photogenerated carriers. Electrochemical impedance spectroscopy (EIS) can be used to study charge transfer and interfacial reaction ability in photocatalytic materials. As shown in Fig. 6d, the EIS Nyquist diagrams of pure g-C_3N_4 and $B_{0.05}$-C_3N_4 were well simulated as equivalent circuits (Fig. 6d inset), where R_s and R_t are the electrolyte solution resistance and the interface charge transfer resistance, respectively. According to this model, the R_t value of $B_{0.05}$-C_3N_4 (6.49 $\times 10^4$ Ω) is significantly lower than that of pure g-C_3N_4 (1.58 $\times 10^5$ Ω), indicating that the introduction of the B-N bond reduces the charge transfer resistance at the photocatalyst interface, which greatly improves the separation and transfer efficiency of photoinduced electron and hole pairs [49].

To ascertain the electron transfer between the prepared catalyst and the adsorbed O_2 on the surface, the differential charge density and the Bader charge (Table S7) were calculated. We denoted the N atom at the adsorption site as N_{ads}, and we can characterize the charge transfer between N_{ads}, surrounding C atoms, doped B atoms, and oxygen molecules by calculating the differential charge density around N_{ads}. In the differential charge density diagram (Fig. 6e and f), isovalue is set to 0.05, yellow region represents electron accumulation, and blue region represents electron depletion. By comparing Fig. 6e and f, it is easy to find that after the B atoms replaced the C atoms to introduce the B-N bond, B atoms act as the capture center of electrons and transfers more electrons to N_{ads} through B-N bond (the yellow area is larger). In addition, for O_2, it can be seen from the differential charge density diagram that when the B-N bond is introduced, the yellow area around O_2 is larger, indicating that N_{ads} transfers more electrons to O_2. This is also confirmed by Bader charge calculations, where the amount of charge transferred from pure g-C_3N_4 and $B_{0.05}$-C_3N_4 to O_2 is 0.024 e^- and 0.084 e^-, respectively. The above DFT calculation results show that after the B atoms replaced the C atoms to introduce the B-N bond, B atom acts as electron capture center, and electrons are transferred to N_{ads} atom through B-N bond. In this way, O_2 adsorbed on N_{ads} atom can obtain more electrons, which is especially beneficial to the generation of ROS.
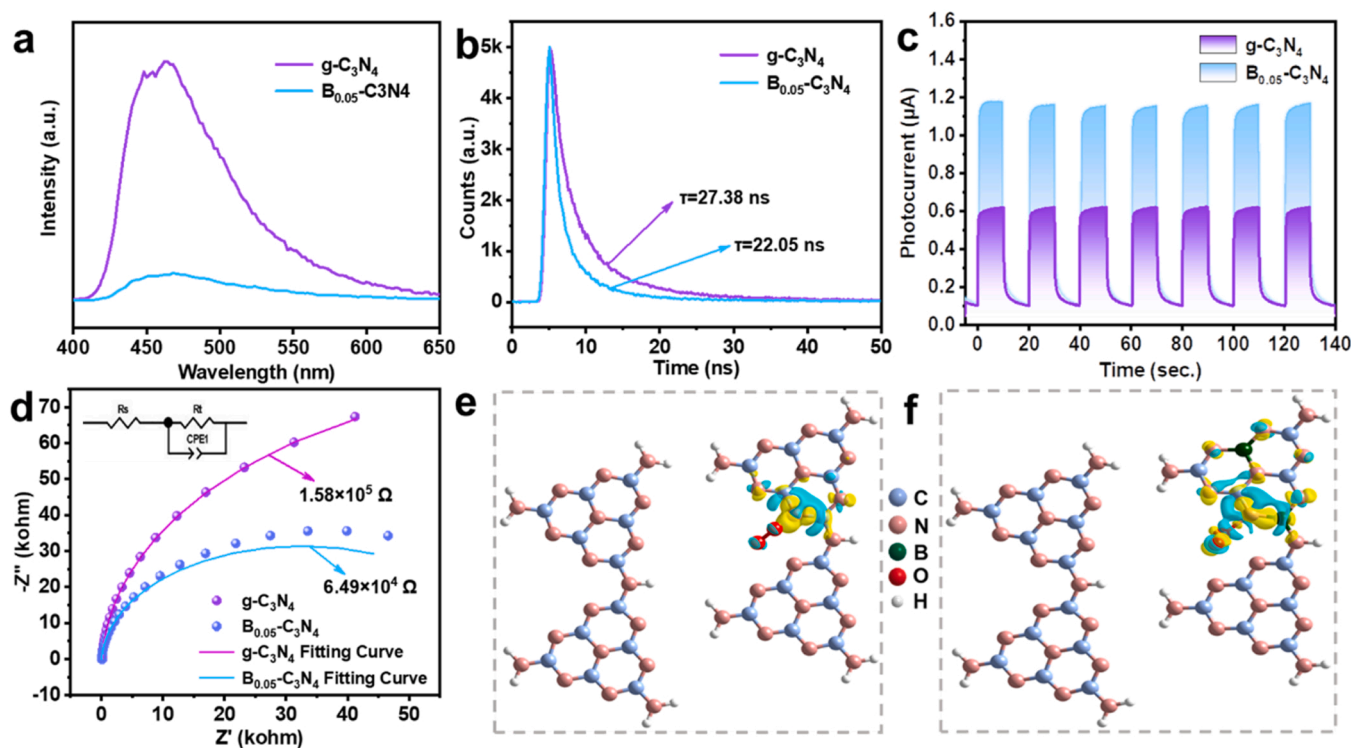
Fig. 6. (a) Steady-state PL spectra, (b) Time-resolved PL spectra, (c) photocurrent responses and (d) EIS Nyquist plots of pure g-C_3N_4 and $B_{0.05}$-C_3N_4. The calculated charge density difference for pure g-C_3N_4 (e) and $B_{0.05}$-C_3N_4 (f) structures, which was calculated by the following equation: $\Delta\rho = \rho(total)-\rho(total-N_{ads})-\rho(N_{ads})$, isovalue= 0.05. Yellow and blue regions represent electron accumulation and depletio.

3.4. Catalytic reaction degradation path and catalyst reusability

Surface redox reaction in the reactive sites is vital to photocatalytic pollutant degradation, and it is generally believed that the HOMO and LUMO act as oxidation and reduction sites, respectively. The electron densities of the LUMO and HOMO of the optimized $B_{0.05}$-C_3N_4 are shown in Fig. S9a and b, the HOMO indicated that the original C-N coordination acted as the strong oxidation site, while the LUMO suggested that B-N coordination provided reduction sites. The O_2 adsorbed to the B-N bond gains electrons to form highly oxidizing ROS to attack pollutants [50–52]. Combining the EPR and DFT results, it can be inferred that the B-N bond is the preferred reaction site for photocatalytic reactions. Although $B_{0.05}$-C_3N_4 can effectively degrade target pollutants, the conversion intermediates produced in the photocatalytic degradation process may be potential environmental pollutants. The molecular frontier orbital theory and the enrichment Fukui function (CFF) based on DFT calculation were used to predict the degradation pathway of RhB. Based on the frontier orbital theory, HOMO and LUMO can describe the positions where organic pollutant molecules are more likely to lose or gain electrons during photodegradation. The optimized chemical structure, HOMO and LUMO orbitals of RhB dye are shown in Figs. 7a,b, respectively. In general, HOMO orbitals indicate that electrons are vulnerable

to escape, most likely to be attacked by free radicals [53]. As shown in Fig. 7b, the HOMO orbital of RhB is mainly located around the chromophore of RhB, indicating that the chromophore is the main site for free radical attack. CFF can more accurately predict the attack sites of free radicals. f^-, f^+ and f^0 are used to describe electrophilic attack, nucleophilic attack and free radical attack of RhB molecule respectively. The higher their values are, the more vulnerable they are to corresponding attack. Fig. 7c and d display partial Fukui index and Fukui index isosurface of RhB molecules (the molecular structure diagram of RhB with atomic number and complete natural population analysis (NPA) charge distribution and Fukui index of RhB are shown in Fig. S10 and Table S8 of the Supporting information), it is not difficult to see that N_3, N_{17}, C_9, C_{11}, C_{12}, C_{13}, C_{15}, O_{24} have higher f^0 values and will become the primary attack sites of ROS ($\bullet O_2^-$ and $^1O_2$). The intermediate products and final products in the degradation process of RhB were identified by HPLC-MS combined technology. The name, molecular formula and m/z of intermediates obtained by HPLC-MS analysis are shown in Table S9. The results of DFT calculation and HPLC-MS analysis indicated that N-de-ethylation, chromophore cracking, ring-opening and mineralization are the main steps of RhB degradation (Fig. 8) [54]. First, the ROS ($\bullet O_2^-$ and $^1O_2$) attack the RhB molecule to make N-ethyl fall off the molecular structure, and produce the deethyl product (R1-R5).

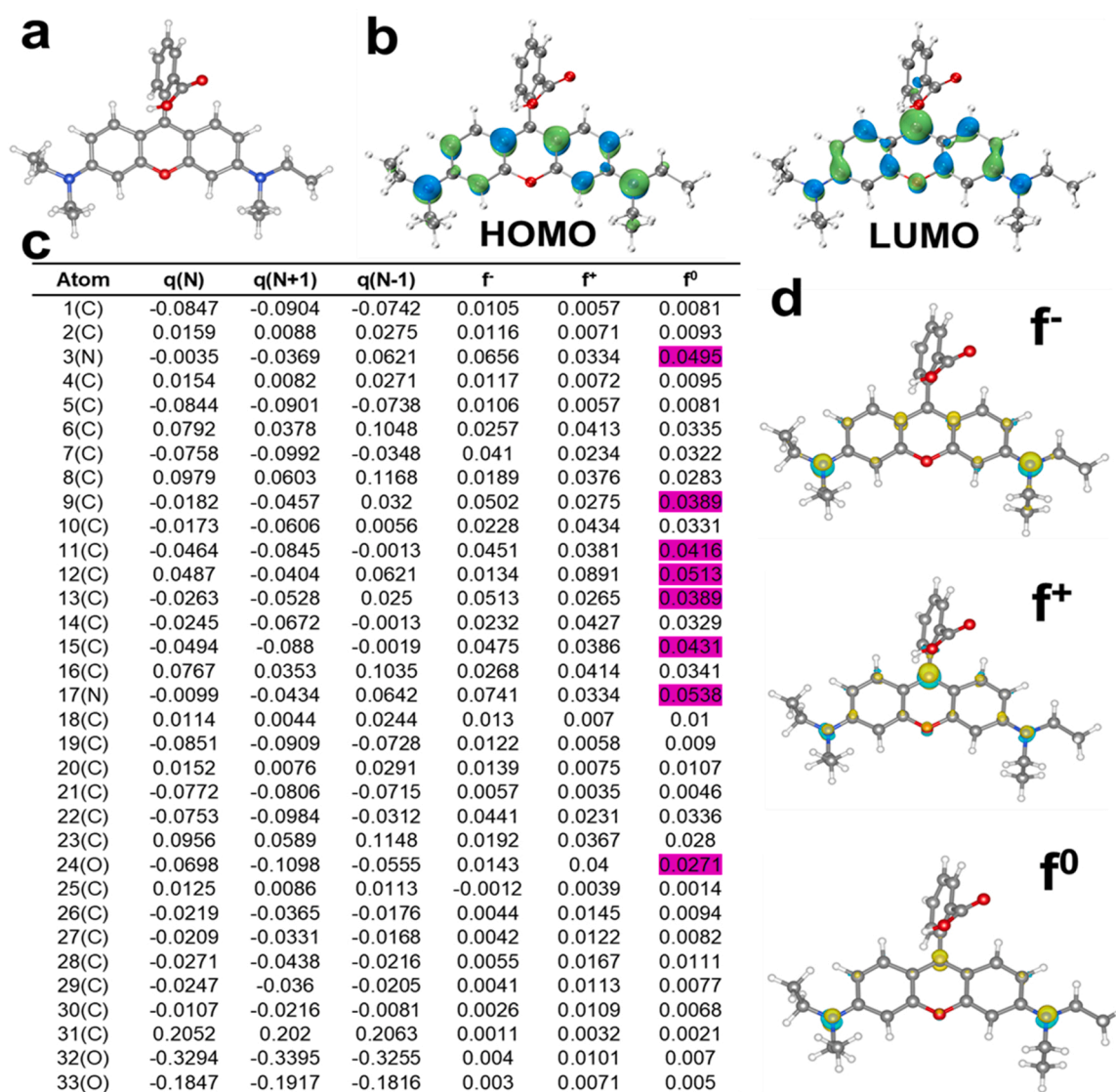| Atom	q(N)	q(N+1)	q(N-1)	f^-	f^+	f^0
1(C)	-0.0847	-0.0904	-0.0742	0.0105	0.0057	0.0081
2(C)	0.0159	0.0088	0.0275	0.0116	0.0071	0.0093
3(N)	-0.0035	-0.0369	0.0621	0.0656	0.0334	0.0495
4(C)	0.0154	0.0082	0.0271	0.0117	0.0072	0.0095
5(C)	-0.0844	-0.0901	-0.0738	0.0106	0.0057	0.0081
6(C)	0.0792	0.0378	0.1048	0.0257	0.0413	0.0335
7(C)	-0.0758	-0.0992	-0.0348	0.041	0.0234	0.0322
8(C)	0.0979	0.0603	0.1168	0.0189	0.0376	0.0283
9(C)	-0.0182	-0.0457	0.032	0.0502	0.0275	0.0389
10(C)	-0.0173	-0.0606	0.0056	0.0228	0.0434	0.0331
11(C)	-0.0464	-0.0845	-0.0013	0.0451	0.0381	0.0416
12(C)	0.0487	-0.0404	0.0621	0.0134	0.0891	0.0513
13(C)	-0.0263	-0.0528	0.025	0.0513	0.0265	0.0389
14(C)	-0.0245	-0.0672	-0.0013	0.0232	0.0427	0.0329
15(C)	-0.0494	-0.088	-0.0019	0.0475	0.0386	0.0431
16(C)	0.0767	0.0353	0.1035	0.0268	0.0414	0.0341
17(N)	-0.0099	-0.0434	0.0642	0.0741	0.0334	0.0538
18(C)	0.0114	0.0044	0.0244	0.013	0.007	0.01
19(C)	-0.0851	-0.0909	-0.0728	0.0122	0.0058	0.009
20(C)	0.0152	0.0076	0.0291	0.0139	0.0075	0.0107
21(C)	-0.0772	-0.0806	-0.0715	0.0057	0.0035	0.0046
22(C)	-0.0753	-0.0984	-0.0312	0.0441	0.0231	0.0336
23(C)	0.0956	0.0589	0.1148	0.0192	0.0367	0.028
24(O)	-0.0698	-0.1098	-0.0555	0.0143	0.04	0.0271
25(C)	0.0125	0.0086	0.0113	-0.0012	0.0039	0.0014
26(C)	-0.0219	-0.0365	-0.0176	0.0044	0.0145	0.0094
27(C)	-0.0209	-0.0331	-0.0168	0.0042	0.0122	0.0082
28(C)	-0.0271	-0.0438	-0.0216	0.0055	0.0167	0.0111
29(C)	-0.0247	-0.036	-0.0205	0.0041	0.0113	0.0077
30(C)	-0.0107	-0.0216	-0.0081	0.0026	0.0109	0.0068
31(C)	0.2052	0.202	0.2063	0.0011	0.0032	0.0021
32(O)	-0.3294	-0.3395	-0.3255	0.004	0.0101	0.007
33(O)	-0.1847	-0.1917	-0.1816	0.003	0.0071	0.005

Fig. 7. (a) Molecule structure of RhB. (b) HOMO and LUMO distribution of RhB. Partial NPA charge distribution and Fukui index (c) and the isosurface of the Fukui index (d) of RhB.
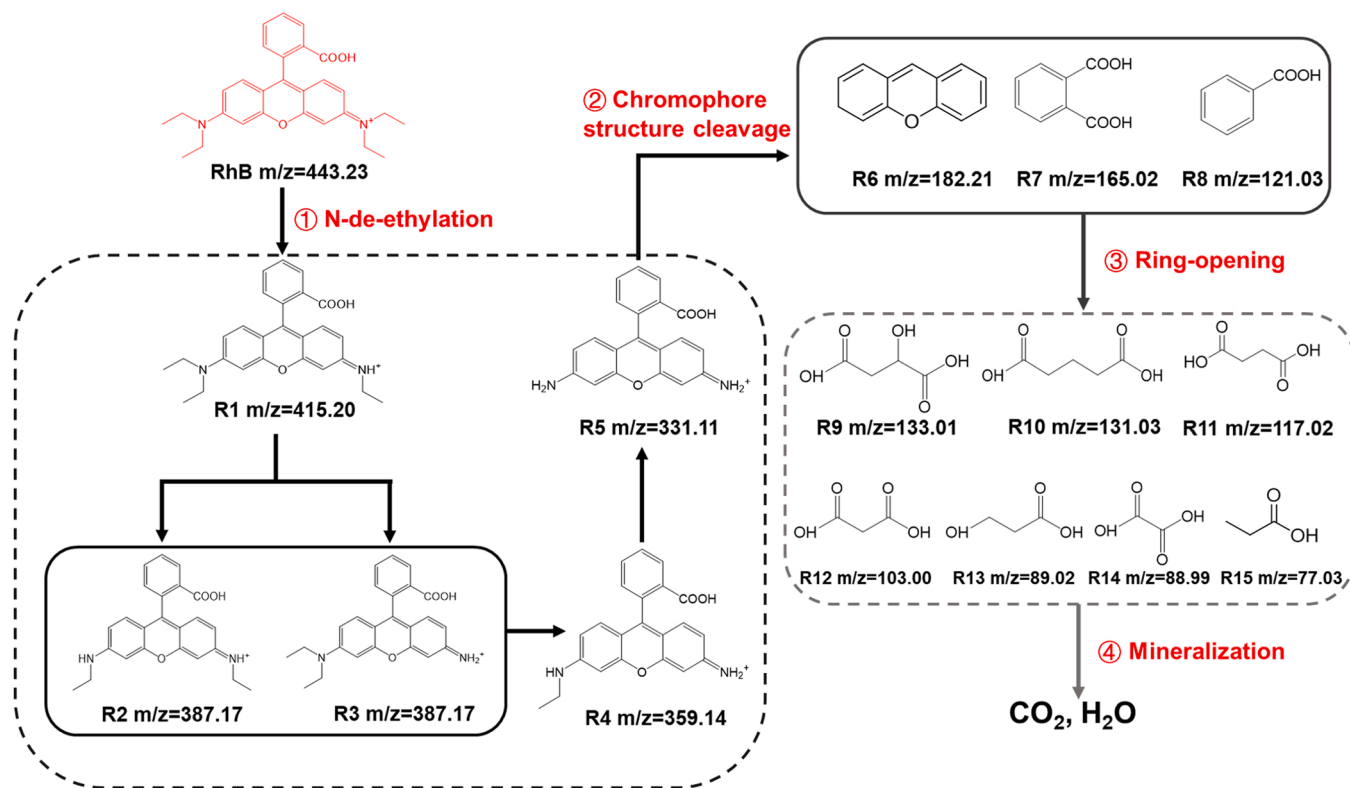
Fig. 8. The degradation pathway of RhB molecules during the photocatalytic process under visible light.
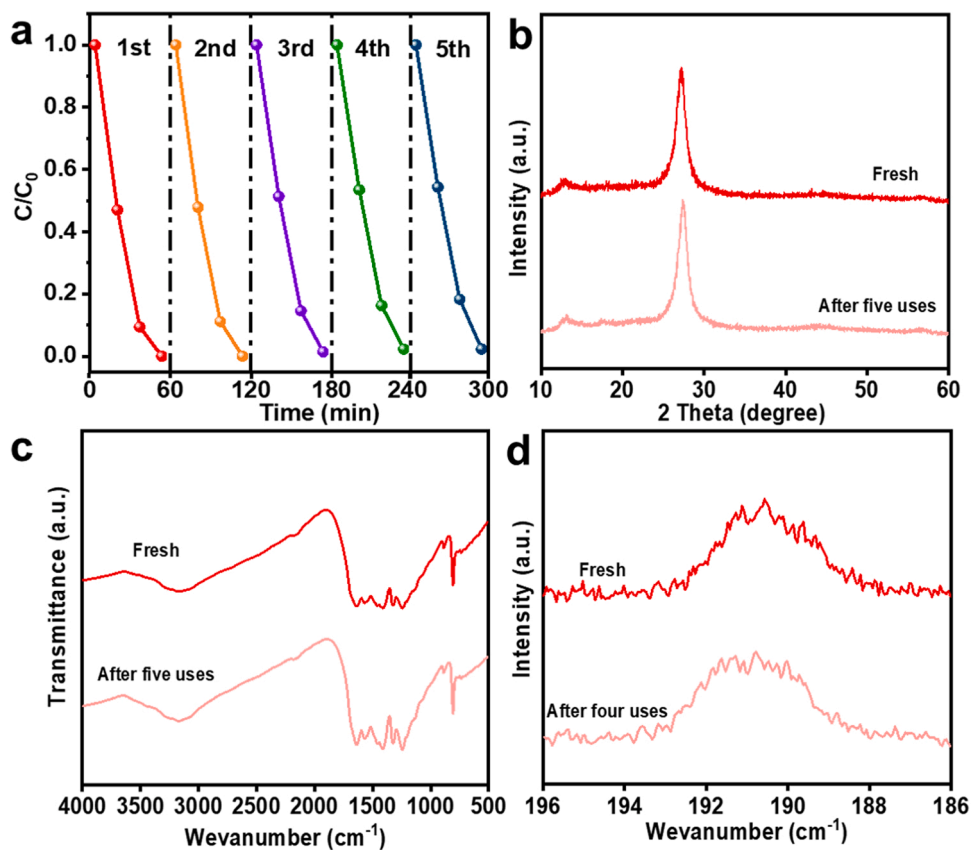

Fig. 9. (a) Cyclic experiments of photocatalytic degradation of RhB. The (b) XRD, (c) FT-IR, (d) B high resolution XPS spectrum of $B_{0.05}$-C_3N_4 were compared before and after five cycles of reaction.

Secondly, the bond between the heteroanthracene group and the phenyl group constituting the chromophore structure is broken as the contaminants are further oxidized, resulting in the decolorization of RhB (R6-R8). With the deepening of the degradation process, the high molecular weight heteroanthracene group and the phenyl group are destroyed to generate low molecular weight acid (R9-R15), and further mineralize into CO_2 and H_2O. The toxicity (the *Daphnia magna* LC50 and developmental toxicity) of RhB and its degradation intermediate were assessed by Toxicity Estimation Software (TEST). As shown in Fig. S11a, the *Daphnia magna* LC50 of all intermediates except P6 is higher than the 8.35 mg/L of RhB, which means that almost all intermediates have lower biological toxicity than RhB. In addition, the developmental toxicity of RhB and degraded intermediates were predicted (Fig. S11b). It is not difficult to see from the figure that the developmental toxicity of all intermediates except intermediate P1 is lower than RhB, and the predicted result of intermediates R7 and R10 are even considered as "developmental non-toxicant". The above results indicate that the toxicity of RhB is effectively reduced during the degradation process, indicating that the g-C_3N_4 with surface B-N bond photocatalytic degradation system is a green and effective degradation strategy.

The reusability and stability of the photocatalyst are particularly important for its actual water treatment applications. To research the reusability of $B_{0.05}$-C_3N_4, five consecutive cycles of RhB degradation experiments were conducted. As shown in Fig. 8a, the photocatalytic degradation activity of $B_{0.05}$-C_3N_4 on RhB hardly decreases within five cycles, which indicates that the prepared g-C_3N_4 with B-N bond photocatalyst has outstanding photocatalytic stability. To verify the stability of the structure of the catalyst after cycle experiment, XRD, FT-IR and XPS analysis were performed on the $B_{0.05}$-C_3N_4 after five cycles of experiments (Fig. 9b, Fig. 9c, and Fig. 9d). These spectra maintained a high degree of consistency before and after cyclic experiments, which verified the structural stability of $B_{0.05}$-C_3N_4. Based on the above analysis, the reusability and stability of the synthesized g-C_3N_4 with B-N bond photocatalyst is worthy of recognition, and it is promising to be used in actual water treatment processes.

4. Conclusions

In this study, we demonstrate that g-C_3N_4 with surface B-N bond ($B_{0.05}$-C_3N_4) has a significant photocatalytic activation of O_2. Based on this, the photocatalytic degradation activity of $B_{0.05}$-C_3N_4 is significantly higher than pure g-C_3N_4. XPS and DFT calculation confirmed that boron atom doping successfully introduced B-N bond into g-C_3N_4, and heightened the adsorption capacity of N atom in B-N bond to O_2. Photochemical test, electrochemical test and DFT calculation research show that the introduction of B-N bond significantly promotes the process of light absorption, charge separation and transfer. The boron atom acts as electron capture centers to transfer electrons to N atoms via B-N bond, while nitrogen atoms transfer electrons and energy to O_2 adsorbed on the surface, generating effective ROS ($\cdot O_2^-$ and $^1O_2$) to attack pollutants, which is also confirmed by quenching experiments and ESR spectroscopy. Benefiting from the efficient generation of $\cdot O_2^-$ and $^1O_2$, the g-C_3N_4 with surface B-N bond exhibits excellent performance in photocatalytic degradation of organic matter. This research comes up with a new idea for accelerating the activation of O_2 and a feasible way for the practical application of photocatalytic technology.

CRediT authorship contribution statement

Haiyin Zhan: Investigation, Writing – original draft, Formal analysis. **Qixing Zhou:** Conceptualization, Supervision, Writing – review & editing, Funding acquisition; **Mingmei Li:** Investigation. **Ruiren Zhou:** Investigation. **Yueshuang Mao:** Investigation. **Pengfei Wang:** Supervision, review & editing.

Declaration of Competing Interest

The authors declare that they have no known competing financial interests or personal relationships that could have appeared to influence the work reported in this paper.

Appendix A. Supporting information

Supplementary data associated with this article can be found in the online version at doi:10.1016/j.apcatb.2022.121329.

References

[1] B.A. Marinho, R.O. Cristóvão, J.M. Loureiro, R.A.R. Boaventura, V.J.P. Vilar, Solar photocatalytic reduction of Cr(VI) over Fe(III) in the presence of organic sacrificial agents, Appl. Catal. B 192 (2016) 208–219, https://doi.org/10.1016/j.apcatb.2016.03.061.

[2] H. Zhan, Y. Wang, X. Mi, Z. Zhou, P. Wang, Q. Zhou, Effect of graphitic carbon nitride powders on adsorption removal of antibiotic resistance genes from water, Chin. Chem. Lett. 31 (2020) 2843–2848, https://doi.org/10.1016/j.cclet.2020.08.015.

[3] K. Li, Y. He, P. Chen, H. Wang, J. Sheng, W. Cui, G. Leng, Y. Chu, Z. Wang, F. Dong, Theoretical design and experimental investigation on highly selective Pd particles decorated C_3N_4 for safe photocatalytic NO purification, J. Hazard. Mater. 392 (2020), 122357, https://doi.org/10.1016/j.jhazmat.2020.122357.

[4] K. Zhao, L. Zhang, J. Wang, Q. Li, W. He, J.J. Yin, Surface structure-dependent molecular oxygen activation of BiOCl single-crystalline nanosheets, J. Am. Chem. Soc. 135 (2013) 15750–15753, https://doi.org/10.1021/ja4092903.

[5] S. Wang, Y. Zhu, X. Luo, Y. Huang, J. Chai, T. Wong, G. Xu, 2D WC/WO_3 heterogeneous hybrid for photocatalytic decomposition of organic compounds with Vis-NIR light, Adv. Funct. Mater. 28 (2018), https://doi.org/10.1002/adfm.201705357.

[6] X. Sun, X. Luo, X. Zhang, J. Xie, S. Jin, H. Wang, X. Zheng, X. Wu, Y. Xie, Enhanced superoxide generation on defective surfaces for selective photooxidation, J. Am. Chem. Soc. 141 (2019) 3797–3801, https://doi.org/10.1021/jacs.8b13051.

[7] Q. Zhou, S. Ma, S. Zhan, Superior photocatalytic disinfection of Ag-3D ordered mesoporous CeO_2 under visible light condition, Appl. Catal. B 224 (2018) 27–37, https://doi.org/10.1016/j.apcatb.2017.10.032.

[8] R. Ossola, O.M. Jonsson, K. Moor, K. McNeill, Singlet oxygen quantum yields in environmental waters, Chem. Rev. 121 (2021) 4100–4146, https://doi.org/10.1021/acs.chemrev.0c00781.

[9] G. Liu, T. Zhang, T. Wang, H. Yamashita, Y. Zhao, X. Qian, Peroxydisulfate activation by photo-generated charges on mesoporous carbon nitride for removal of chlorophenols, Appl. Catal. B 296 (2021), 120370, https://doi.org/10.1016/j.apcatb.2021.120370.

[10] Y. Dai, C. Li, Y. Shen, T. Lim, J. Xu, Y. Li, H. Niemantsverdriet, F. Besenbacher, N. Lock, R. Su, Light-tuned selective photosynthesis of azo- and azoxy-aromatics using graphitic C_3N_4, Nat. Commun. 9 (2018) 60, https://doi.org/10.1038/s41467-017-02527-8.

[11] S. Ma, S. Zhan, Y. Jia, Q. Shi, Q. Zhou, Enhanced disinfection application of Ag-modified g-C_3N_4 composite under visible light, Appl. Catal. B 186 (2016) 77–87, https://doi.org/10.1016/j.apcatb.2015.12.051.

[12] L. Bai, H. Huang, S. Zhang, L. Hao, Z. Zhang, H. Li, L. Sun, L. Guo, H. Huang, Y. Zhang, Photocatalysis-assisted Co_3O_4/g-C_3N_4 p-n junction all-solid-state supercapacitors: a bridge between energy storage and photocatalysis, Adv. Sci. 7 (2020) 2001939, https://doi.org/10.1002/advs.202001939.

[13] P. Wang, Y. Mao, L. Li, Z. Shen, X. Luo, K. Wu, P. An, H. Wang, L. Su, Y. Li, S. Zhan, Unraveling the interfacial charge migration pathway at the atomic level in a highly efficient Z-scheme photocatalyst, Angew. Chem. Int. Ed. 58 (2019) 11329–11334, https://doi.org/10.1002/anie.201904571.

[14] B.R. Bhagat, A. Dashora, Understanding the synergistic effect of Co-loading and B-doping in g-C_3N_4 for enhanced photocatalytic activity for overall solar water splitting, Carbon 178 (2021) 666–677, https://doi.org/10.1016/j.carbon.2021.03.049.

[15] G. Zuo, S. Liu, L. Wang, H. Song, P. Zong, W. Hou, B. Li, Z. Guo, X. Meng, Y. Du, T. Wang, V.A.L. Roy, Finely dispersed Au nanoparticles on graphitic carbon nitride as highly active photocatalyst for hydrogen peroxide production, Catal. Commun. 123 (2019) 69–72, https://doi.org/10.1016/j.catcom.2019.02.011.

[16] Y. Li, M. Gu, T. Shi, W. Cui, X. Zhang, F. Dong, J. Cheng, J. Fan, K. Lv, Carbon vacancy in C3N4 nanotube: Electronic structure, photocatalysis mechanism and highly enhanced activity, Appl. Catal. B 262 (2020), 118281, https://doi.org/10.1016/j.apcatb.2019.118281.

[17] J. Zhang, M. Zhang, L. Lin, X. Wang, Sol processing of conjugated carbon nitride powders for thin-film fabrication, Angew. Chem. Int. Ed. 54 (2015) 6297–6301, https://doi.org/10.1002/anie.201501001.

[18] Z. Zhou, Z. Shen, C. Song, M. Li, H. Li, S. Zhan, Boosting the activation of molecular oxygen and the degradation of tetracycline over high loading Ag single atomic catalyst, Water Res. 201 (2021), 117314, https://doi.org/10.1016/j.watres.2021.117314.

[19] X. Xiao, Y. Gao, L. Zhang, J. Zhang, Q. Zhang, Q. Li, H. Bao, J. Zhou, S. Miao, N. Chen, J. Wang, B. Jiang, C. Tian, H. Fu, A promoted charge separation/transfer system from Cu single atoms and C3N4 layers for efficient photocatalysis, Adv. Mater. 32 (2020), e2003082, https://doi.org/10.1002/adma.202003082.

[20] P. Wang, Z. Shen, Y. Xia, H. Wang, L. Zheng, W. Xi, S. Zhan, Atomic insights for optimum and excess doping in photocatalysis: a case study of few-layer Cu-ZnIn2S4, Adv. Funct. Mater. 29 (2019) 1807013, https://doi.org/10.1002/adfm.201807013.

[21] X. Yu, P. Han, Z. Wei, L. Huang, Z. Gu, S. Peng, J. Ma, G. Zheng, Boron-doped graphene for electrocatalytic N2 reduction, Joule 2 (2018) 1610–1622, https://doi.org/10.1016/j.joule.2018.06.007.

[22] J. Ren, P. Innocenzi, 2D boron nitride heterostructures: recent advances and future challenges, Small Struct. 2 (2021) 2100068, https://doi.org/10.1002/sstr.202100068.

[23] Y. Min, C. Dou, H. Tian, J. Liu, L. Wang, Isomers of B←N-fused dibenzo-azaacenes: how B←N affects opto-electronic properties and device behaviors? Chem. Eur. J. 27 (2021) 4364–4372, https://doi.org/10.1002/chem.202004615.

[24] X. Zhang, D. Kim, X. Guo, Y. Zhu, L.Y.S. Lee, Impacts of boron doping on the atomic structure, stability, and photocatalytic activity of Cu3P nanocrystals, Appl. Catal. B 298 (2021), 120515, https://doi.org/10.1016/j.apcatb.2021.120515.

[25] X. Wang, K. Maeda, A. Thomas, K. Takanabe, G. Xin, J.M. Carlsson, K. Domen, M. Antonietti, A metal-free polymeric photocatalyst for hydrogen production from water under visible light, Nat. Mater. 8 (2009) 76–80, https://doi.org/10.1038/nmat2317.

[26] H. Yu, R. Shi, Y. Zhao, T. Bian, Y. Zhao, C. Zhou, G.I.N. Waterhouse, L.Z. Wu, C. H. Tung, T. Zhang, Alkali-assisted synthesis of nitrogen deficient graphitic carbon nitride with tunable band structures for efficient visible-light-driven hydrogen evolution, Adv. Mater. 29 (2017) 1605148, https://doi.org/10.1002/adma.201605148.

[27] J. Li, D. Wu, J. Iocozzia, H. Du, X. Liu, Y. Yuan, W. Zhou, Z. Li, Z. Xue, Z. Lin, Achieving efficient incorporation of pi-electrons into graphitic carbon nitride for markedly improved hydrogen generation, Angew. Chem. Int. Ed. 58 (2019) 1985–1989, https://doi.org/10.1002/anie.201813119.

[28] S. Zhang, L. Gao, D. Fan, X. Lv, Y. Li, Z. Yan, Synthesis of boron-doped g-C3N4 with enhanced electro-catalytic activity and stability, Chem. Phys. Lett. 672 (2017) 26–30, https://doi.org/10.1016/j.cplett.2017.01.046.

[29] J. Li, X. Wang, L. Huang, L. Tian, M. Shalom, C. Xiong, H. Zhang, Q. Jia, S. Zhang, F. Liang, Ultrathin mesoporous graphitic carbon nitride nanosheets with functional cyano group decoration and nitrogen-vacancy defects for an efficient selective CO2 photoreduction, Nanoscale 13 (2021) 12634–12641, https://doi.org/10.1039/d1nr02639a.

[30] W. Wang, H. Zhou, Y. Liu, S. Zhang, Y. Zhang, G. Wang, H. Zhang, H. Zhao, Formation of B-N-C coordination to stabilize the exposed active nitrogen atoms in g-C3N4 for dramatically enhanced photocatalytic ammonia synthesis performance, Small 16 (2020), e1906880, https://doi.org/10.1002/smll.201906880.

[31] C. Huang, C. Chen, M. Zhang, L. Lin, X. Ye, S. Lin, M. Antonietti, X. Wang, Carbon-doped BN nanosheets for metal-free photoredox catalysis, Nat. Commun. 6 (2015) 7698, https://doi.org/10.1038/ncomms8698.

[32] K. Chu, Q. Li, Y. Liu, J. Wang, Y. Cheng, Filling the nitrogen vacancies with sulphur dopants in graphitic C3N4 for efficient and robust electrocatalytic nitrogen reduction, Appl. Catal. B 267 (2020), 118693, https://doi.org/10.1016/j.apcatb.2020.118693.

[33] H.L. Meng, S.Y. Lin, J.J. Feng, L. Zhang, A.J. Wang, Coordination regulated pyrolysis synthesis of ultrafine FeNi/(FeNi)9S8 nanoclusters/nitrogen, sulfur-codoped graphitic carbon nanosheets as efficient bifunctional oxygen electrocatalysts, J. Colloid Interface Sci. 610 (2022) 573–582, https://doi.org/10.1016/j.jcis.2021.11.101.

[34] R.M. Sun, L. Zhang, J.J. Feng, K.M. Fang, A.J. Wang, In situ produced Co9S8 nanoclusters/Co/Mn-S, N multi-doped 3D porous carbon derived from eriochrome black T as an effective bifunctional oxygen electrocatalyst for rechargeable Zn-air batteries, J. Colloid Interface Sci. 608 (2022) 2100–2110, https://doi.org/10.1016/j.jcis.2021.10.144.

[35] C. Chen, D. Yan, Y. Wang, Y. Zhou, Y. Zou, Y. Li, S. Wang, BN pairs enriched defective carbon nanosheets for ammonia synthesis with high efficiency, Small 15 (2019), e1805029, https://doi.org/10.1002/smll.201805029.

[36] Y. Mao, P. Wang, L. Li, Z. Chen, H. Wang, Y. Li, S. Zhan, Unravelling the synergy between oxygen vacancies and oxygen substitution in BiO2−x for efficient molecular-oxygen activation, Angew. Chem. Int. Ed 59 (2020) 3685–3690, https://doi.org/10.1002/anie.201914001.

[37] D. Zhao, Y. Wang, C.L. Dong, Y.C. Huang, J. Chen, F. Xue, S. Shen, L. Guo, Boron-doped nitrogen-deficient carbon nitride-based Z-scheme heterostructures for photocatalytic overall water splitting, Nat. Energy 6 (2021) 388–397, https://doi.org/10.1038/s41560-021-00795-9.

[38] F. Yang, D. Liu, Y. Li, L. Cheng, J. Ye, Salt-template-assisted construction of honeycomb-like structured g-C3N4 with tunable band structure for enhanced photocatalytic H2 production, Appl. Catal. B 240 (2019) 64–71, https://doi.org/10.1016/j.apcatb.2018.08.072.

[39] Z. Wang, Y. Huang, M. Chen, X. Shi, Y. Zhang, J. Cao, W. Ho, S.C. Lee, Roles of N-vacancies over porous g-C3N4 microtubes during photocatalytic NOx removal, ACS Appl. Mater. Interfaces 11 (2019) 10651–10662, https://doi.org/10.1021/acsami.8b21987.

[40] J. Liao, W. Cui, J. Li, J. Sheng, H. Wang, X. Dong, P. Chen, G. Jiang, Z. Wang, F. Dong, Nitrogen defect structure and NO+ intermediate promoted photocatalytic NO removal on H2 treated g-C3N4, Chem. Eng. J. 379 (2020), 122282, https://doi.org/10.1016/j.cej.2019.122282.

[41] Y. Nosaka, A.Y. Nosaka, Generation and detection of reactive oxygen species in photocatalysis, Chem. Rev. 117 (2017) 11302–11336, https://doi.org/10.1021/acs.chemrev.7b00161.

[42] H. Wang, W. Wu, M. Feng, W. Tu, T. Xiao, T. Xiong, H. Ang, X. Yuan, J.W. Chew, Visible-light-driven removal of tetracycline antibiotics and reclamation of hydrogen energy from natural water matrices and wastewater by polymeric carbon nitride foam, Water Res. 144 (2018) 215–225, https://doi.org/10.1016/j.watres.2018.07.025.

[43] M.K. Bhunia, K. Yamauchi, K. Takanabe, Harvesting solar light with crystalline carbon nitrides for efficient photocatalytic hydrogen evolution, Angew. Chem. Int. Ed. 53 (2014) 11001–11005, https://doi.org/10.1002/anie.201405161.

[44] G.P. Mane, S.N. Talapaneni, K.S. Lakhi, H. Ilbeygi, U. Ravon, K. Al-Bahily, T. Mori, D.H. Park, A. Vinu, Highly ordered nitrogen-rich mesoporous carbon nitrides and their superior performance for sensing and photocatalytic hydrogen generation, Angew. Chem. Int. Ed. 56 (2017) 8481–8485, https://doi.org/10.1002/anie.201702386.

[45] L.K. Putri, B.J. Ng, W.J. Ong, H.W. Lee, W.S. Chang, S.P. Chai, Engineering nanoscale p–n junction via the synergetic dual-doping of p-type boron-doped graphene hybridized with n-type oxygen-doped carbon nitride for enhanced photocatalytic hydrogen evolution, J. Mater. Chem. A 6 (2018) 3181–3194, https://doi.org/10.1039/c7ta09723a.

[46] G. Liu, G. Zhao, W. Zhou, Y. Liu, H. Pang, H. Zhang, D. Hao, X. Meng, P. Li, T. Kako, J. Ye, In situ bond modulation of graphitic carbon nitride to construct p-n homojunctions for enhanced photocatalytic hydrogen production, Adv. Funct. Mater. 26 (2016) 6822–6829, https://doi.org/10.1002/adfm.201602779.

[47] X. Shi, M. Fujitsuka, S. Kim, T. Majima, Faster electron injection and more active sites for efficient photocatalytic H2 evolution in g-C3N4/MoS2 hybrid, Small 14 (2018), e1703277, https://doi.org/10.1002/smll.201703277.

[48] L. Shi, L. Yang, W. Zhou, Y. Liu, L. Yin, X. Hai, H. Song, J. Ye, Photoassisted construction of holey defective g-C3N4 photocatalysts for efficient visible-light-driven H2O2 production, Small 14 (2018) 1703142, https://doi.org/10.1002/smll.201703142.

[49] Y. Yu, W. Yan, X. Wang, P. Li, W. Gao, H. Zou, S. Wu, K. Ding, Surface Engineering for extremely enhanced charge separation and photocatalytic hydrogen evolution on g-C3N4, Adv. Mater. 30 (2018) 1705060, https://doi.org/10.1002/adma.201705060.

[50] H. Wang, W. Wu, M. Feng, W. Tu, T. Xiao, T. Xiong, H. Ang, X. Yuan, J.W. Chew, Visible-light-driven removal of tetracycline antibiotics and reclamation of hydrogen energy from natural water matrices and wastewater by polymeric carbon nitride foam, Water Res. 144 (2018) 215–225, https://doi.org/10.1016/j.watres.2018.07.025.

[51] H. Wang, J. Zhang, X. Yuan, L. Jiang, Q. Xia, H. Chen, Photocatalytic removal of antibiotics from natural water matrices and swine wastewater via Cu(I) coordinately polymeric carbon nitride framework, Chem. Eng. J. 392 (2020), 123638, https://doi.org/10.1016/j.cej.2019.123638.

[52] H. Dou, L. Chen, S. Zheng, Y. Zhang, G.Q. Xu, Band structure engineering of graphitic carbon nitride via Cu2+/Cu+ doping for enhanced visible light photoactivity, Mater. Chem. Phys. 214 (2018) 482–488, https://doi.org/10.1016/j.matchemphys.2018.04.071.

[53] K. Cheng, Z. Cai, J. Fu, X. Sun, W. Sun, L. Chen, D. Zhang, W. Liu, Synergistic adsorption of Cu(II) and photocatalytic degradation of phenanthrene by a jaboticaba-like TiO2/titanate nanotube composite: an experimental and theoretical study, Chem. Eng. J. 358 (2019) 1155–1165, https://doi.org/10.1016/j.cej.2018.10.114.

[54] Y. Pang, L. Kong, D. Chen, G. Yuvaraja, S. Mehmood, Facilely synthesized cobalt doped hydroxyapatite as hydroxyl promoted peroxymonosulfate activator for degradation of Rhodamine B, J. Hazard. Mater. 384 (2020), 121447, https://doi.org/10.1016/j.jhazmat.2019.121447.